

Probing multiple populations of compact binaries with third-generation gravitational-wave detectors

Ken K. Y. Ng,^{1,2,*} Salvatore Vitale,^{1,2} Will M. Farr,^{3,4} and Carl L. Rodriguez⁵

¹*LIGO Laboratory, Massachusetts Institute of Technology, Cambridge, Massachusetts 02139, USA*

²*Kavli Institute for Astrophysics and Space Research, Massachusetts Institute of Technology, Cambridge, Massachusetts 02139, USA*

³*Department of Physics and Astronomy, Stony Brook University, Stony Brook, New York, 11794, USA*

⁴*Center for Computational Astrophysics, Flatiron Institute, 162 Fifth Avenue, New York 10010, USA*

⁵*McWilliams Center for Cosmology, Department of Physics, Carnegie Mellon University, 5000 Forbes Ave, Pittsburgh, Pennsylvania 15213, USA*

(Dated: January 3, 2022)

Third-generation (3G) gravitational-wave (GW) detectors will be able to observe binary-black-hole mergers (BBHs) up to redshift of ~ 30 . This gives unprecedented access to the formation and evolution of BBHs throughout cosmic history. In this paper we consider three sub-populations of BBHs originating from the different evolutionary channels: isolated formation in galactic fields, dynamical formation in globular clusters and mergers of black holes formed from Population III (Pop III) stars at very high redshift. Using input from populations synthesis analyses, we created two months of simulated data of a network of 3G detectors made of two Cosmic Explorers and an Einstein Telescope, consisting of ~ 16000 field and cluster BBHs as well as ~ 400 Pop III BBHs. First, we show how one can use non-parametric models to infer the existence and characteristic of a primary and secondary peak in the merger rate distribution. In particular, the location and the height of the secondary peak around $z \approx 12$, arising from the merger of Pop III remnants, can be constrained at $\mathcal{O}(10\%)$ level. Then we perform a modeled analysis, using phenomenological templates for the merger rates of the three sub-population, and extract the branching ratios and the characteristic parameters of the merger rate densities of the individual formation channels. With this modeled method, the uncertainty on the measurement of the fraction of Pop III BBHs can be improved to $\lesssim 10\%$, while the ratio between field and cluster BBHs can be measured with an uncertainty of $\sim 50\%$.

I. INTRODUCTION

Advanced gravitational-wave (GW) detectors such as LIGO [1], Virgo [2] and Kagra [3] have dramatically increased our ability to study stellar mass black holes and the environments in which they form. The latest catalog released by the LIGO-Virgo-Kagra (LVK) collaboration includes 39 new GW detections, most of which are binary black holes (BBHs), bringing the total number of stellar mass black holes detected with GWs to over 100 [4, 5]. These observations have already allowed for interesting astrophysical measurements [4–7], such as hints for multiple formation channels [8–14], hierarchical mergers [15–21], as well as constraints on stellar physics [22–24], primordial BHs [25–30] and ultralight bosons [31–34]. Therefore, the growing set of BBHs enable studying both the properties of individual sources, as well as those of the underlying populations.

One of the key questions that can be addressed by GW astrophysics is how many such populations exist, and what are their characteristics. Multiple approaches have been proposed to address these questions, which ultimately rely on looking for features that would be expected in the BBH generated by each channel, such as their mass and spin distribution [8, 17, 35–46], eccentricity

distribution [47] or redshift distribution [48, 49]. However, due to the limited sensitivity of current GW detectors, the observed BBHs are relatively “local”, with redshift $z \lesssim 1$ [4–7, 50, 51]. Even as LIGO, Virgo and Kagra improve their sensitivities with the implementation of frequency dependent quantum squeezing [52], and better low-frequency isolation [53], the detectors horizon will reach $z \sim 3$ only for the heaviest systems [54, 55].

Second-generation detectors will therefore be unable to access mergers at redshifts larger than a few. This likely precludes the possibility of detecting binaries whose component black holes originated directly from the Population III (Pop III) stars, whose formation peak could be as high as $z \sim 10$. Primordial black holes [56–60], might also be out of reach for existing facilities¹. This will not be the case in the era of third-generation (3G) GW detectors such as Cosmic Explorer (CE) [65, 66] and Einstein Telescope (ET) [67–69]. In fact, 3G detectors will have horizons up to $z \gtrsim 30$ and enable accessing most of the BBHs throughout the cosmic history [55]. Therefore, both detections and not-detections of high redshift BBHs with 3G detectors can provide significant constraints on the properties of Pop III remnants. This is particularly important as the remnants of Pop III stars might be the light

¹ We note that there are studies suggesting the heaviest BBH detected in the first part of LIGO/Virgo O3 run - GW190521 [61, 62] - may be a Pop III BBH [63, 64].

* kenkyng@mit.edu

seeds that led the formation of supermassive black holes early in cosmic history [70]. Whereas the space-based gravitational-wave detector LISA [71] and electromagnetic missions such as the X-ray observatory Lynx [72] might reveal the presence of heavy (i.e. $M \gtrsim 100 M_{\odot}$) black holes at redshifts of 10, ground-based 3G detectors might very well be the only way to searching for smaller building blocks: stellar mass black holes.

Using the current *local* BBH merger rate estimate, $\sim 25 \text{ Gpc}^{-3} \text{ yr}^{-1}$ [7], we project that ~ 10000 BBHs per month merge in the universe, assuming the merger rate follows the same evolution as the star formation rate (SFR) [73]. Nearly all of these BBHs would be detectable by 3G detectors, and most of which will also have very high signal-to-noise ratio (SNR), leading to very precise distance (and hence redshift, assuming a known cosmology) measurements [74–76]. The large number of loud observations thus allows inferring the morphology of merger rate densities, in both parametric and non-parametric ways [77–80]. In Vitale *et al.* [78], we showed how combining redshift measurements of tens of thousands of GW observations in 3G detectors and assuming all BBHs are formed in galactic fields, one can infer the SFR history and the time-delay distribution. In light of the properties of the BBHs detected by LIGO and Virgo in the last few years, it has become harder to assume that all black holes are formed in galactic fields, since many of the black holes being detected are consistent with having formed dynamically, in globular or nuclear clusters or in the disks of active galactic nuclei (AGN) [81–89]. In this paper, we greatly extend our previous work [78] and explore the possibility of simultaneously identifying and constraining the properties of *multiple* formation channels. In particular, we simulate universes where black holes can be formed in galactic fields, globular clusters and Pop III stars. We show how well one can constrain the properties of each channel, and their branching ratios. In particular, we focus the evidence for a high-redshift ($z \gtrsim 5$) population, which would be the smoking gun of formation outside of the traditional evolutionary pathways. The rest of this paper is structured as follows: we first introduce the astrophysical formation channels in Sec. II, then briefly review the Bayesian statistical methods used for the analysis in Sec. III and the simulation setup in Sec. IV. After going through the results in Sec. V, we discuss their possible implications in Sec. VI.

II. ASTROPHYSICAL MODELS

In this section we summarize the main astrophysical properties of the BBH formation channels that we consider in the paper. Astrophysical BBHs are believed to form in various environments, such as binary stellar evolution in galactic fields [90–98], dynamical formation through multi-body interactions in star clusters (from low-mass stars to large nuclear star clusters) [13, 99–105] or AGN disk [81–89], from Population III (Pop III) stars [56–59]

or primordial black holes [25–30, 60, 106, 107].

For simplicity, in this paper we use galactic fields and globular cluster as the only main populations at low redshift, and Pop III stars as the only high-redshift channel. The analysis can be easily extended to even more population, at the price of an increased computational cost. Hereafter, we label the BBHs in the three formation channels as *field binaries*, *cluster binaries* and *Pop III binaries*. Since an astrophysical BH is a remnant of stellar collapse, the merger rate history of each channel is correlated with the SFR and with the time delay from the binary formation to merger. Cluster and field binaries consist of BH-remnants leftover from Pop I/II stars, whose corresponding SFR peaks at late times: $z \sim 3$ [108, 109]. Accounting for the typically time delay between binary formation and merger ($\sim 10 \text{ Myr}$ to $\sim 10 \text{ Gyr}$), their merger rates is expected to peak at around $z \sim 2$ [92, 95, 96, 103].

Pop III stars are instead formed at early times, $z \gtrsim 10$, from primordial gas clouds at extremely low metallicity [108, 110]. The “metal-free” environment reduces the stellar wind mass loss during the binary evolution [111] so that Pop III stars might be more massive than the most recent stellar populations. Eventually, heavy BH remnants are left behind that merge in a short timescale, resulting on a merger rate density that could peak at around $z \sim 10$ [56, 57, 59, 95].

The fact that different formation channels result in different merger rate distributions as a function of redshift, especially for Pop III remnants, can be exploited to infer properties of BBH populations solely based on the redshift distribution of the detected sources. Obviously, more elaborated tests can be envisaged, that also rely on other distinguishing features, e.g. masses, spins or eccentricity of the sources. In this study we will show that tests based on the redshift distribution alone can already provide significant constraints, while also having the benefit of being model-independent, at least in some of the implementations we demonstrate below. This seems particularly desirable, since the true distribution of intrinsic parameters such as masses and spins is highly uncertain, especially for Pop III remnants.

In Fig. 1 we show the “true” merger rate densities of three formation channels we use in this study, and focus on key features of their shapes (we will discuss later the branching ratios, i.e. the relative scale). The rate densities of field (orange), cluster (blue) and Pop III (green) binaries are phenomenological fits (details in Appendix B, Eqs. (B1), (B2) and (B3)) of the population synthesis simulation from Refs. [58, 95, 103], respectively. We notice that the high-redshift tail of the cluster merger rate density is much steeper than that of the field binaries. This is largely due to the choice of model: the cluster merger rates are based on the model of globular cluster formation from [113], which goes to zero at $z \sim 10$. That, combined with the delay between cluster formation and BBH mergers (since BHs in clusters can only merge after the cluster has formed *and* the BHs have sunk to the center due to dynamical friction, a process which can take

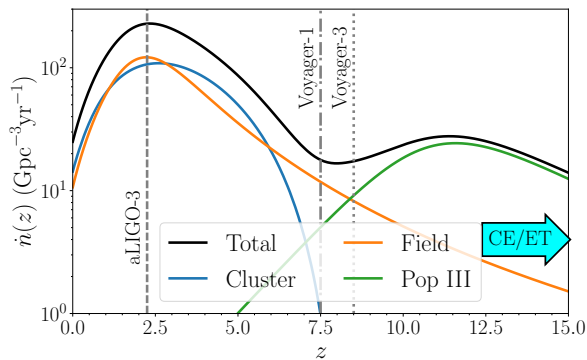


FIG. 1. The merger rate densities of field (orange), cluster (blue) and Pop III (green) binaries, together with the overall merger rate (black), given by the sum of the three populations. For the purposes of this plot, field and cluster merger rate densities are normalized such that they produce the same number of binaries up to z of 15. The Pop III merger rate density is scaled so that its peak has an amplitude of $1/10$ relative to the peak of the field and cluster merger rate densities. The vertical lines indicate the detector horizons, z_h , to BBHs with total masses (in the source frame) $\leq 100M_\odot$, in a network of three advanced detectors ($z_h \sim 2.25$), a single Voyager [112] ($z_h \sim 8.5$) and a network of three Voyager-like detectors ($z_h \sim 12.1$), respectively [55]. The SNR threshold for detection is set to be 8 for a single detector and 12 for a detector network.

$\sim 100\text{Myr}$ [e.g., 114]) causes a steeper slope in the merger rate at high z . The field and cluster merger rate densities peak at similar values, $z \sim 2.2$ and $z \sim 2.6$, respectively, whereas the Pop III merger rate density peaks much later, at $z \sim 11.6$.

The vertical lines in Fig. 1 report the horizon of future ground-based detector networks. Advanced detectors network can observe BBHs up to the low-redshift peak of the merger rate densities of the two dominating channels, field and clusters. However, as the plot shows, for $z \lesssim 2$, the merger rate densities of both field and cluster binaries are quite similar. Hence advanced detectors are unlikely to be able to disentangle the two channels using only redshift information (as mentioned above, one can use other features, at the price of making more model-dependent in the analysis). The situation improves with a single Voyager detector (“Voyager-1” line), which can access most of the field and cluster binaries up to $z \lesssim 8$ and therefore exploit the expected difference in their merger rate after the peak to characterize the two channels. A network of 3 Voyager-like detectors (“Voyager-3” line) can extend the horizon to a redshift where the contribution to the total merger rate of the field and the Pop III channel might becomes comparable. However, it is only with 3G detectors that one can access the peak of the merger rate from Pop III. In fact, the horizon of CE and ET to heavy BBHs is outside of the range of Fig. 1 (as indicated by the cyan arrow in the bottom right corner), at $z \sim 100$. As we will show in the following sections the fact that the horizon of 3G detectors extends well beyond the expected

peak of Pop III mergers allows for both modeled and unmodeled tests of the existence of such subpopulation.

III. STATISTICAL MODELS

Here, we briefly review the main statistical tool used in the analysis, i.e. the hierarchical Bayesian inference framework [115–119]. We model the production mechanism of BBHs as an inhomogeneous Poisson process whose differential merger rate

$$\frac{d\dot{N}}{dz}(z | \mathbf{\Lambda}, \dot{N}),$$

depends on a set of “shape parameters” $\mathbf{\Lambda}$ and an overall scale factor given by the total merger rate: $\dot{N} = \int \frac{d\dot{N}}{dz} dz$. The vector of shape parameters $\mathbf{\Lambda}$ contains the quantities which are used to model the underlying physical populations (see Sec. IV).

One can write the hyper-posterior of the population parameters $\mathbf{\Lambda}$ and \dot{N} given a set of N_{obs} observations $\mathbf{d} \equiv \{d_i\}_{i=1}^{N_{\text{obs}}}$ as:

$$\begin{aligned} & p(\mathbf{\Lambda}, \dot{N} | \mathbf{d}) \\ & \propto \left[\prod_{i=1}^{N_{\text{obs}}} T \int dz_i p(d_i | z_i) \frac{d\dot{N}}{dz}(z_i | \mathbf{\Lambda}, \dot{N}) \right] e^{-\dot{N}T} \pi(\mathbf{\Lambda}, \dot{N}) \\ & \simeq \left[\prod_{i=1}^{N_{\text{obs}}} T \frac{1}{M_i} \sum_{j=1}^{M_i} \frac{d\dot{N}}{dz}(z_{ij} | \mathbf{\Lambda}, \dot{N}) \right] e^{-\dot{N}T} \pi(\mathbf{\Lambda}, \dot{N}), \end{aligned} \quad (1)$$

In going from the second to the last line we have approximated the integrals with discrete sums. For the i -th source, this amounts to calculating an average of the merger rate evaluated at the M_i points $\{z_{ij}\}_{j=1}^{M_i}$ drawn from the likelihood $p(d_i | z_i)$ of the i -th source.

In the third line, $\pi(\mathbf{\Lambda}, \dot{N})$ is the hyper-prior, and T is the observation time interval. In the study, we follow two approaches to construct $d\dot{N}/dz$: (i) a “nonparametric” approach that utilizes Gaussian process regression (GPR) to infer $d\dot{N}/dz$ as a piecewise function over several redshift bins [120]; and (ii) a “parametric” approach in which we assume phenomenological functions to model various subpopulations [115].

In the parametric approach, we define a volumetric merger rate density in the source frame of k -th subpopulation, $\dot{n}_k(z) \equiv d\dot{N}_k/dV_c$, with dV_c/dz being the differential comoving volume. Then, the merger rate history $d\dot{N}_k/dz$ in the detector frame as a function of redshift for the k -th subpopulation is:

$$\frac{d\dot{N}_k}{dz}(z | \mathbf{\Lambda}_k, \dot{N}_k) = \frac{1}{1+z} \frac{dV_c}{dz} \dot{n}_k(z | \mathbf{\Lambda}_k, \dot{N}_k), \quad (2)$$

where \dot{N}_k and $\mathbf{\Lambda}_k$ are the integrated merger rate and the vector of hyper-parameters of k -th population, respectively. The $1/(1+z)$ term accounts for the cosmological time dilation. The total merger density can be expressed as the sum of the individual number densities for all sub-populations, i.e.

$$\frac{d\dot{N}}{dz}(z | \mathbf{\Lambda}, \mathcal{N}) = \sum_k \frac{d\dot{N}_k}{dz}(z | \mathbf{\Lambda}_k, \dot{N}_k), \quad (3)$$

where the vectors $\mathbf{\Lambda}$ and \mathcal{N} contains all $\mathbf{\Lambda}_k$'s and \dot{N}_k 's, respectively. In addition, $\sum_k \dot{N}_k = \dot{N}$. We may rewrite Eq. (3) in terms of the branching ratios, i.e. the fraction of sources in each sub-population, $f_k \equiv \dot{N}_k/\dot{N}$,

$$\frac{d\dot{N}}{dz}(z | \mathbf{\Lambda}, \dot{N}) = \dot{N} \sum_k f_k p_k(z | \mathbf{\Lambda}_k), \quad (4)$$

where $p_k(z | \mathbf{\Lambda}_k)$ is the normalized merger rate of the k -th population, and the f_k 's are subject to the constraint $\sum_k f_k = 1$. Since we expect the fraction of Pop III binaries to be small, it is more convenient to introduce the fraction of cluster binaries over the sum of field and cluster binaries, $\tilde{f}_G \equiv f_G/(f_G + f_F)$.

Therefore, for the parametrized analysis we model the merger rates of the three subpopulations in terms of several phenomenological parameters, which are treated as unknowns, together with the branching ratios (Sec. IV). The total merger rate in Eq. 1 is thus calculated by adding up the contribution of each channel. On the other hand, in the unmodeled approach, we measure $\frac{d\dot{N}}{dz}(z | \mathbf{\Lambda}, \dot{N})$ directly, without making any assumption about the individual subpopulations that might be contributing to it.

More details on the two approaches can be found in Appendices A and B, whereas the hyper-priors are described in the Appendix C. Throughout the study, we assume Planck 15 cosmology [121].

IV. SIMULATION DETAILS

In this section we describe how we prepare the simulated universes that will be analyzed with the methods described in the previous section.

First, we need to choose reference (i.e. “true”) merger rate densities that will be used to generate the redshift of the BBHs. We do so by mean of the phenomenological curves in Eqs. (B1), (B2) and (B3). As described in Appendix B, these curves describe the morphology of each volumetric merger rate density, and are parametrized by, e.g., the rising slope at low redshift, the declining slope at high redshift, and the redshift at which the merger rate peaks. The phenomenological curves are obtained by fitting Eqs. (B1), (B2) and (B3) to the simulation results available in the literature [58, 95, 103]. Specifically, we take the model-averaged simulation results of Refs. [95]

and [103] for field and cluster binaries, respectively, as well as “FS1” model’s result of [58] for Pop III binaries.

We use the following numbers as the “true” values of the each curve parameters, when preparing our sources:

$$\begin{aligned} (\hat{\alpha}_F, \hat{\beta}_F, \hat{C}_F) &= (2.57, 5.83, 3.36), \\ (\hat{\mu}_G, \hat{\sigma}_G, \hat{t}_G) &= (1.63, 0.96, 0.59 \text{ Gyr}), \\ (\hat{\alpha}_{\text{III}}, \hat{b}_{\text{III}}, \hat{z}_{\text{III}}) &= (0.66, 0.3, 11.6). \end{aligned}$$

While this fixes the true shape of the merger rate for each subpopulation, we still need to fix the amplitudes. We use 9 different values of the merger rate between cluster and field binaries, \tilde{f}_G , equally spaced in the range from 0 to 1. For each value of \tilde{f}_G , we consider two universes: one with and one without Pop III binaries.

Following the latest GWTC-2 result, we fix the local volumetric merger rate density to $\dot{n}(0) = 25 \text{ Gpc}^{-3}\text{yr}^{-1}$ [7]. This yields $\dot{N}_F + \dot{N}_G \approx 8000$ per month. In the universes with Pop III binaries, the Pop III fraction $f_{\text{III}} \approx 0.024$ is chosen to generate an additional 200 sources per month coming from the Pop III channel. This number is chosen such that the peak merger rate density of Pop III binaries is ~ 10 times smaller than the peak of the dominating channels. The nominal value of this peak, $\dot{n}_{\text{III}}(z_{\text{III}}) \approx 20 \text{ Gpc}^{-3}\text{yr}^{-1}$, is consistent with the comparison of “FS1” model to the Pop I/II field binaries in Ref. [95]. We stress that the current predictions for the Pop III merger rate span a few orders of magnitudes, in either direction, relative to the one we are using [56, 57, 59, 95]. This is because the formation efficiency of Pop III binaries greatly depends on the initial mass function of the Pop III stars and the distribution of the initial orbital separation (see Refs. [59, 95]). Since \dot{n}_{III} declines rapidly at later cosmic time, it does not significantly contribute to $\dot{n}(0)$.

To ensure a reasonable measurement of luminosity distance, which typically requires three or more detectors, we choose a baseline detector network with one CE in Australia, one CE in the United States, and one ET in Europe [74–76]. Generally speaking, not all BBHs within the detector horizon can be detected with SNRs over some thresholds, depending on their orientation and intrinsic parameters. This results in a Malmquist bias [116, 119]. However, the deficiency drops to 50% at $z \sim 20$ for a typical $30M_{\odot} - 30M_{\odot}$ BBH. Therefore, we limit our analysis to the redshift range $0 \leq z \leq 15$ and neglect selection effect.

Finally, we simulate a month of data in the following way. We first draw the set of true redshifts, $\{z_{\text{true}}\}$, from the “true” $d\dot{N}/dz$ in each universe. Then, for each $z_{\text{true},i}$, we obtain the *observed* redshift, $z_{\text{obs},i}$, by drawing a random variable from a mock-up single-event likelihood conditional on $z_{\text{true},i}$. Following [78], we approximate the likelihood for redshift as a lognormal distribution conditional on $z_{\text{true},i}$ with a standard deviation $\sigma_{\text{LN},i} = 0.017z_{\text{true},i}$. Finally, we draw 100 single-event likelihood samples condi-

tionAL on $z_{\text{obs},i}$ with the same $\sigma_{\text{LN},i}$ calculated previously. The second step is necessary in order to generate a scattering to the true value within the probable range of the single-event likelihood function. Otherwise, the alignment of the true value and the mean of the likelihood introduces systematic bias in the analysis.

To summarize, we generate 18 simulated universe. In all universes, we generate 16000 (two-months worth data) BBHs from field and cluster binaries with a given branching ratio \tilde{f}_G , and add 400 more Pop III observations for the 9 universes containing Pop III binaries.

V. RESULTS

With the simulations set up in each of the 18 universe as described in the previous section, we now report on the measurement of the total merger rate density (and of each individual population, for the phenomenological mixture model).

A. Gaussian Process Regression

Figure 2 shows our inference on the volumetric merger rate \dot{n} obtained with the unmodeled GPR approach. The black colored bands report the 68% and 95% credible intervals for the universes without (left panel) and with (right panel) Pop III binaries. The colored lines show the true volumetric merger rate of the individual populations. For both of the panels the branching ratio between field and cluster binaries is $\tilde{f}_G = 0.5$. We find that the true \dot{n} 's (black dashed lines) lie within the 95% credible intervals in both cases. While the relative uncertainty on \dot{n} is at a percent level at $z \lesssim 6$, it increases to $\mathcal{O}(100\%)$ at $z \gtrsim 8$. This is because (i) the SNR of each source decreases with the distance, and (ii) the number of sources in each redshift bin is decreasing as the differential comoving volume shrinks at earlier times in the history of the universe.

Perhaps the most attractive feature of the unmodeled analysis, is that we can find some evidence for the presence of an high-redshift subpopulation, even without strong modeling. The simplest way of doing this is to look for local peak(s) in \dot{n} . At the very minimum, we would expect to find evidence for the ‘‘main’’ peak at $z \sim 2$, arising from the merger in fields and clusters, while high-redshift peaks would be indicative of a different subpopulation.

We implement this peak finder algorithm simply by asking that the first derivative is zero and the second is negative: $d\dot{n}/dz = 0$ and $d^2\dot{n}/dz^2 < 0$. Some care is required to avoid false positives due to natural oscillations in the results of the GRP which are not due to astrophysical maxima (or minima) but only to the underlying Gaussian process. These are particularly visible at high redshifts in Fig. 2(a). To mitigate the effect of these fluctuation and suppress the unphysical peaks, we require the height of any high redshift peaks to be at least 1/10 of the height of the low redshift peak, as well as an intra-peak separation

larger than $\Delta z = 1$. These requirements are based on the expected excess of Pop III as discussed in Sec. IV and arguably represent the only modeling involved in the GRP approach that we describe.

With these two restrictions, we count the number of peaks N_{peak} for each \dot{n} sample of the GRP in every simulated universe. The results are shown in Fig. 3 as a function of the true branching ratio cluster/field. For the universes without Pop III binaries, we recover a single peak, as expected, with $> 99\%$ probability (purple histograms). This implies the non-existence of a secondary peak whose relative height is $\geq 10\%$ of the primary peak. On the other hand, the true value for the number of peaks, $N_{\text{peak}} = 2$, is found at $\gtrsim 90\%$ credibility for in the universes with Pop III binaries (orange histograms).

We observe that in the universes with Pop III binaries the posterior on the number of peaks has a secondary mode at $N_{\text{peak}} = 3$ for \tilde{f}_G . We explain this as follows: for $\tilde{f}_G \lesssim 0.5$, the field binaries are the dominating channel, and as clear in Fig. 2 produce a flatter high-redshift tail than the cluster channel. Hence it is easier to produce multiple peaks due to fluctuation and induces a leakage to $N_{\text{peak}} \geq 3$. On the other hand, when $\tilde{f}_G \gtrsim 0.5$, the cluster binaries are dominating and don't contribute to the merger rate at $z \gtrsim 8$ where Pop III population becomes the only source of BBHs, which makes the high-redshift peak spaker and hence easier to reveal. But the Poisson fluctuation of the high-redshift bins in $d\dot{N}/dz$ may still lead to an underestimation of the relative height below our 10% threshold, inducing a small contamination at $N_{\text{peak}} = 1$. We note that the above trend is subject to the model uncertainty of our chosen simulation data in the high-redshift region.

This method also allows measuring the location(s) of the peak(s), which would be useful to understand the population properties. For instance, the shift of the primary peak relative to the star formation rate could inform the typical time delay to merger and a hint of metallicity evolution [100, 122]. In addition, constraining the high redshift peak to $z \gtrsim 8$ would provide support to the existence of Pop III binaries.

We first show the inferred distribution of the low redshift peak, z_l , for all universes in Fig. 4. All measurements of z_l constrain the low redshift peaks to $z < 3$, with 95% credible-interval uncertainties of $\sim 40\%$. The true values are contained within the uncertainty.

Next, we look at the measurements of the high redshift peak's location z_h for the universes with Pop III binaries, as shown by the red violins in Fig. 5. In all cases, the true value $\hat{z}_h = 11.6$ lies within the 95% credible intervals. The lower bound of the credible interval is above $z \sim 7$ for all values of \tilde{f}_G , indicating that one can confidently place the secondary peak at redshift much larger than where the start formation peaks. The width of the credible intervals decrease from $\sim 50\%$ to $\sim 25\%$ when \tilde{f}_G increases from 0 to 1. This may be again explained by the steeper redshift tail in the cluster population, which makes the Pop III peak easier to resolve.

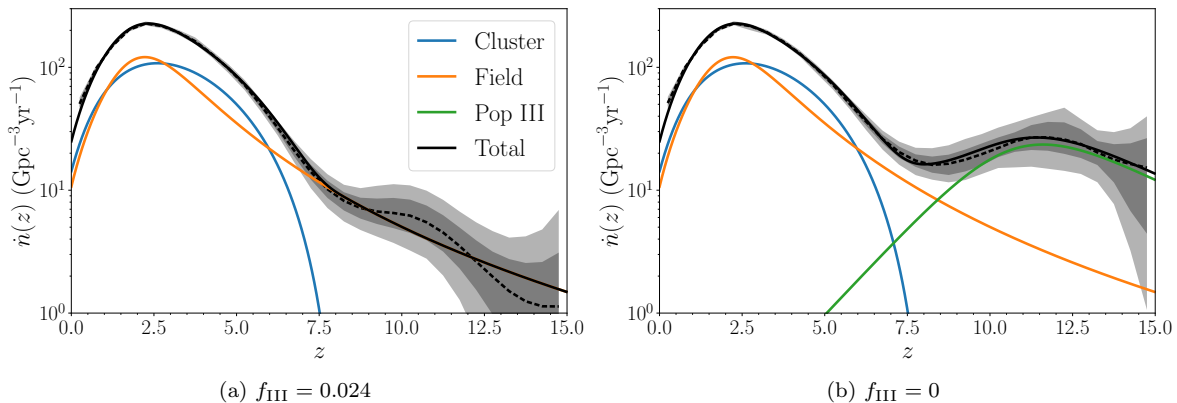


FIG. 2. Reconstruction of \dot{n} for the $\tilde{f}_G = 0.5$ universes with (left panel) and without (right panel) using GPR. The black color band and solid line shows the 68% (darker color) and 95% (lighter color) credible intervals, and the median of recovered \dot{n} , respectively. The black, orange and blue dashed lines are the fiducial \dot{n} , \dot{n}_F , and \dot{n}_G , respectively. Since we cannot model each subpopulation with the nonparametric approach, no hyper-posterior can be drawn for each branch.

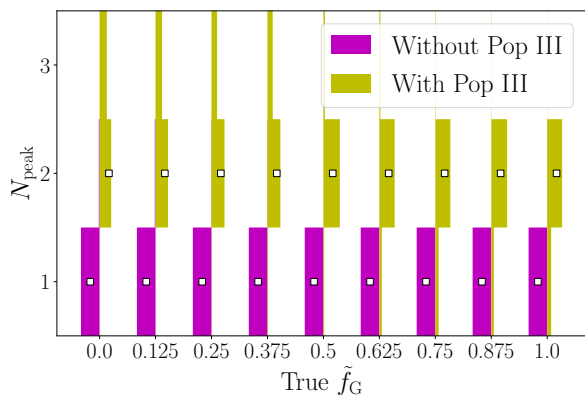


FIG. 3. Posterior distributions of N_{peak} of \dot{n} for all 18 universes. Since N_{peak} is a discrete measure, the distributions are represented by histograms. For the universes without (purple) and with (yellow) Pop III binaries, the true N_{peak} are 1 and 2, respectively.

B. Phenomenological recovery

Having shown how a simple non-parametric model can already provide insight into the existence of an high-redshift population of BBHs, we now repeat the hierarchical inference using the phenomenological model described in Sec. III. The quantities that are measured, their meaning and the priors are fully described in Appendix B and C.

We start by showing the posteriors on the peak of the merger rate density for the Pop III BBHs, this time obtained as one of the parameters on which their phenomenological model depends, in Fig. 5, green violins. Remembering that the orange violins in the same plot reports the measurement we obtained with the GPR approach, we find that the two methods yield very consistent results, with the widths of 95% credible intervals varying

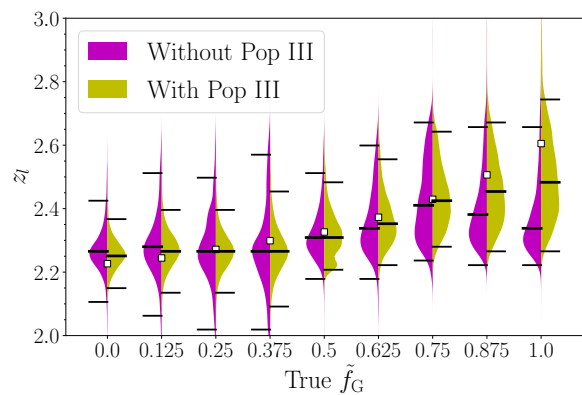


FIG. 4. Hyper-posterior of z_1 for all 18 universes. In each half-leaf, the upper and lower black dashes mark the 95% credible interval, and the middle black dash locates the median. The square markers indicate the true values of z_1 .

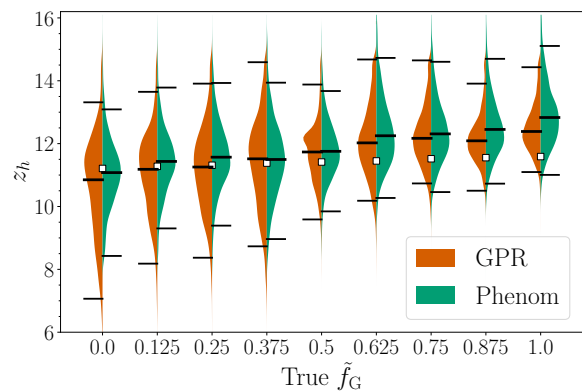


FIG. 5. Hyper-posterior of z_h for the 9 universes with Pop III binaries, conditioned with $\dot{n}(z_h) \geq 0.1\dot{n}(z_1)$ inferred by the GPR model (red) and the phenomenological (Phenom) model (green). Other plot settings are the same as Fig. 4.

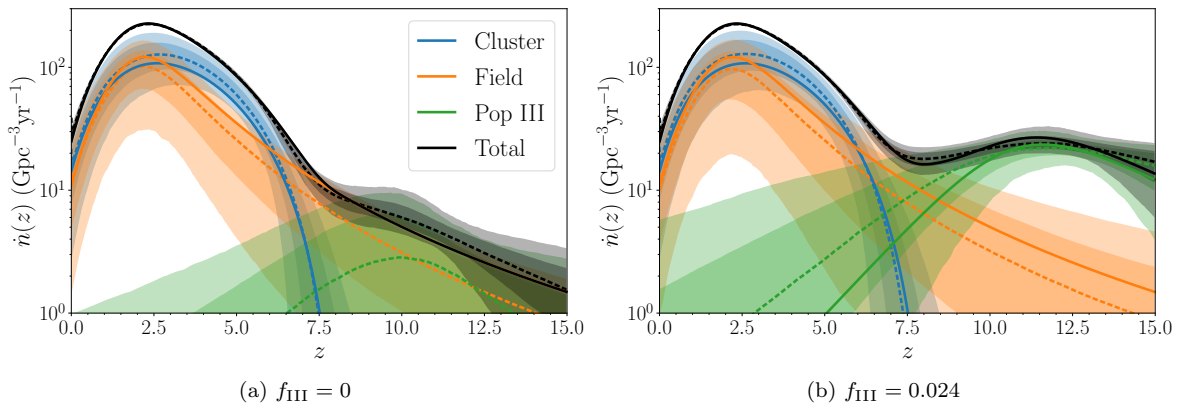


FIG. 6. Reconstruction of merger rate densities for the $\tilde{f}_G = 0.5$ universes without (left panel) and with (right panel) using phenomenological models. The orange, blue, green and black solid lines are the medians of the recovered \dot{n}_F , \dot{n}_G , \dot{n}_{III} and \dot{n} , respectively. The corresponding color bands are the 68% (darker colors) and 95% (lighter colors) credible intervals of the reconstruction. The true merger rate densities are shown as the dashed lines of the same colors. The green dashed line is invisible since there are no Pop III binaries in this universe.

by $\sim 10\%$ at most. The consistency between the two approaches highlights the promise of the nonparametric approach in revealing the existence and location of an high-redshift population. However, as we have emphasized, the phenomenological model directly describes the morphology of each sub-population and thus allows extracting information about each individual population, which cannot be accessed by the nonparametric approach.

In Fig. 6 we show the inferred \dot{n} for the simulated $\tilde{f}_G = 0.5$ universes without (left panel) and with (right panel) Pop III binaries². For each population, the solid line represents the true merger rate, whereas the dashed line and the colored bands represents the median, and the 68%/95% credible intervals.

The total \dot{n} (black colored band) can be well constrained within a few percent level up to $z \sim 6$. For $f_{\text{III}} = 0$, the relative uncertainty rises to $\sim 100\%$ at $z \gtrsim 10$. Even at low redshift, the uncertainty of \dot{n}_F (orange color band) and \dot{n}_G (blue color band) is about 50%, ~ 10 times larger than that of the total rate, \dot{n} . This is because the morphology of \dot{n}_F and \dot{n}_G is similar at $z \lesssim 3$, where most of the BBHs can be detected with a precise distance measurement. Conversely, \dot{n}_F and \dot{n}_G are easier to distinguish at $z \gtrsim 5$ where, as discussed before, \dot{n}_G is declining more rapidly than \dot{n}_F , which instead has a long tail at $z \gtrsim 8$. Overall, the similarity in the morphology of the low-redshift volumetric merger rate of the two dominating channels induces degeneracies, hence boosts uncertainties, in the the individual merger rates, \dot{n}_F and \dot{n}_G .

Considering now the universe with $f_{\text{III}} = 0.024$ (right panel), we find that rate of the Pop III curve, (green colored band) near its peak at $z \sim 12$ can be measured with a relative uncertainty of $\sim 50\%$, while the uncertainty

of other channels remains similar to the universe with $f_{\text{III}} = 0$.

We compare the phenomenological recovery of the total \dot{n} to the GPR recovery (Fig. 2) for the same universes, and find that the typical uncertainty of \dot{n} is smaller by a factor of ~ 2 . This is not surprising, since the phenomenological approach uses models for the subpopulations, which inform the recovery of the overall merger rate. Naturally, the price to pay for the improved precision is to have made the results depend on the goodness of the models.

Next, we look at the hyper-posteriors, i.e. at the posteriors of the variables that parametrize the individual subpopulations, as well as the branching ratios. First, we show the hyper-posterior of the dominating channels' parameters for the universe with $(\tilde{f}_G, f_{\text{III}}) = (0.5, 0)$ (the same of Fig. 6(a)) in Fig. 7. Most of the shape parameters are measured with $\sim 50\%$ uncertainty, e.g. $\tilde{f}_G = 0.59^{+0.28}_{-0.27}$. We note that there are a few interesting correlated pairs, such as (t_G, \tilde{f}_G) and (t_G, σ_G) . Since t_G characterizes the start of the merging cluster binaries, an earlier t_G shifts the peak of cluster population towards higher redshift where the cosmological volume is smaller. Hence the \tilde{f}_G is larger to keep the same number of cluster binaries. On the other hand, a smaller t_G tends to shift cluster population towards lower redshift. Then a larger σ_G is necessary to maintain a wide merger rate peak.

Next, we look at the hyper-posterior of the Pop III merger rate parameters for the same universe, as shown by the purple contours in Fig. 8. We are able to constrain $f_{\text{III}} \lesssim 0.02$. Both a_{III} and b_{III} are very close to their priors, which make sense since f_{III} is small which implies no information about \dot{n}_{III} can be gained. On the other hand, the position of the peak, z_{III} , is shifted towards lower values relative to its prior to suppress the contribution from \dot{n}_{III} to the high-redshift total merger rate, which in this universe is entirely determined by the field binaries.

As a comparison, we now focus on the result for the uni-

² These are the same two universes of Fig. 2

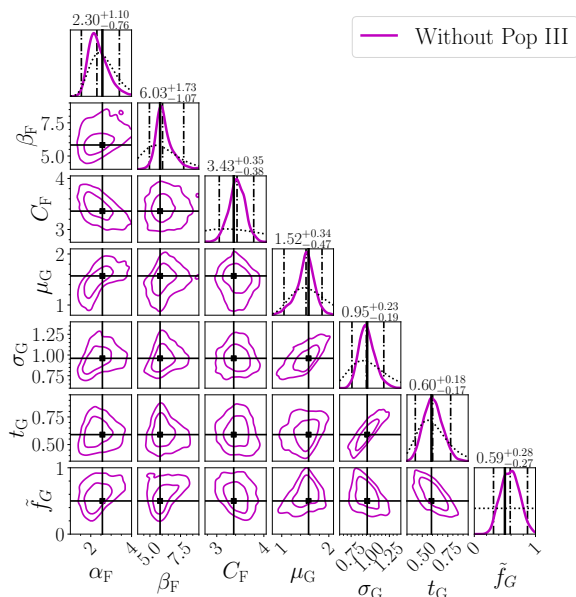


FIG. 7. Hyper-posterior of the dominating channels' hyper-parameters, $(\alpha_F, \beta_F, C_F, \mu_G, \sigma_G, t_G, \tilde{f}_G)$, for the universe with $(\tilde{f}_G, f_{\text{III}}) = (0.5, 0)$ (the same of Fig. 6(a)). For each marginalized 1D posterior (purple solid line in each diagonal slot), the left and right black dashed-dotted lines mark the 95% highest posterior density credible interval, the middle black dashed-dotted line locates the median, and the black dotted line shows the prior. The numerical values of median values and 95% credible intervals are reported above the diagonal slots. The off-diagonal slots show the marginalized 2D posteriors, with the contours representing the 68% and 95% credible intervals. The black markers and solid lines indicate the true values, which lie within the 68% credible interval. The statistical behavior for the universe with Pop III is very similar.

verse with $f_{\text{III}} = 0.024$] (this is the same as in Fig. 6(b)). In Fig. 8, the orange contours show the hyper-posterior of \dot{n}_{III} 's parameters. While the shape parameters of a_{III} and b_{III} are still not well constrained, the peak $z_{\text{III}} = 11.75_{-1.91}^{+1.92}$ is measured with $\sim 30\%$ relative uncertainty. Importantly, $f_{\text{III}} = 0$, i.e., the absence of a Pop III channel, is excluded from the 95% credible interval of the marginalized f_{III} posterior. This provides strong evidence of the existence of Pop III binaries in our simulated data.

It is worth looking at the correlations between the hyper-parameters of the the various subpopulations. Some correlation should be expected since for example the number of sources at high redshift might be explained by the model either with a larger fraction of field binaries, which have a fat high-redshift tail, or by binaries in the Pop III channel. In Fig. 9, we show the marginalized 2D contours of the $(\tilde{f}_G, f_{\text{III}})$ pair for the universes $\tilde{f}_G = 0.5$ without (purple) and with (yellow) Pop III. A positive correlation between the two parameters is clearly visible. This is caused by the partial model degeneracy between \dot{n}_F and \dot{n}_{III} . This goes exactly in the direction one would expect: underestimating f_{III} means that the model must increase

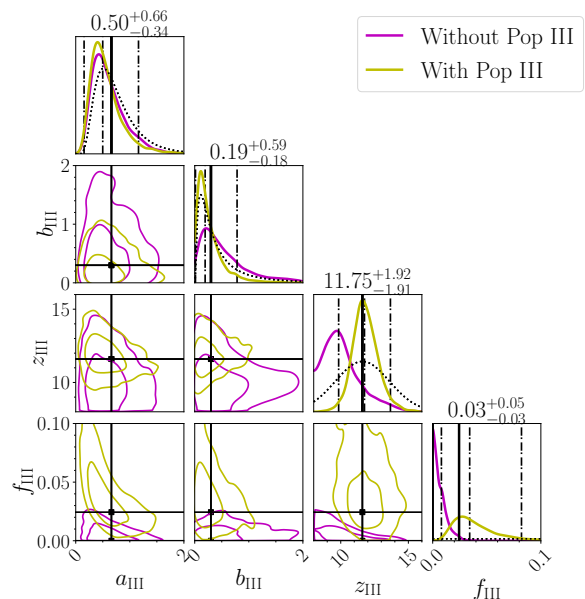


FIG. 8. Hyper-posterior of the Pop III population's hyper-parameters, $(a_{\text{III}}, b_{\text{III}}, z_{\text{III}}, f_{\text{III}})$, for the universes $(\tilde{f}_G, f_{\text{III}}) = (0.5, 0)$ (purple) and $(\tilde{f}_G, f_{\text{III}}) = (0.5, 0.024)$ (yellow). The plot setting is the same as in Fig. 7. Only the medians and 95% credible intervals (orange) are indicated by the dashed-dotted lines and reported above the diagonal slots.

the number of field binaries to account at least partially for the high-redshift binaries. But if the number of field binaries increases, \tilde{f}_G must decrease.

The partial correlation between \dot{n}_F and \dot{n}_{III} manifests itself in two other interesting ways. First, we observe an increase in the uncertainty of \tilde{f}_G when Pop III mergers are present. In Fig. 10, we show violin plots for the marginalized \tilde{f}_G posteriors at different true \tilde{f}_G values. The purple and yellow violins correspond to the universes with and without Pop III binaries, respectively. While the true values lie inside the 95% credible interval in all cases, the uncertainties increase by $\sim 10\%$ for the universes with Pop III binaries.

Second, the uncertainty in f_{III} decreases as \tilde{f}_G increases. Figure 11 is a plot similar to Fig. 10, but showing the marginalized f_{III} posteriors in different universes. When Pop III binaries are present, the uncertainty stays roughly constant $\Delta f_{\text{III}} \sim 0.1$ up to $\tilde{f}_G \lesssim 0.5$, after which it drops gradually to $\Delta f_{\text{III}} \sim 0.05$ at $\tilde{f}_G = 1$. A similar trend is observed when no Pop III binaries exist: the uncertainty drops from $\sim 2.5\%$ to $\lesssim 0.1\%$. This is because \dot{n}_F has a longer tail in the high redshift $z \gtrsim 8$, and is easier to be confused with a small excess of Pop III population.

VI. DISCUSSIONS AND CONCLUSIONS

In this paper, we have shown that observations made by a network of 3G detectors can be used to infer the

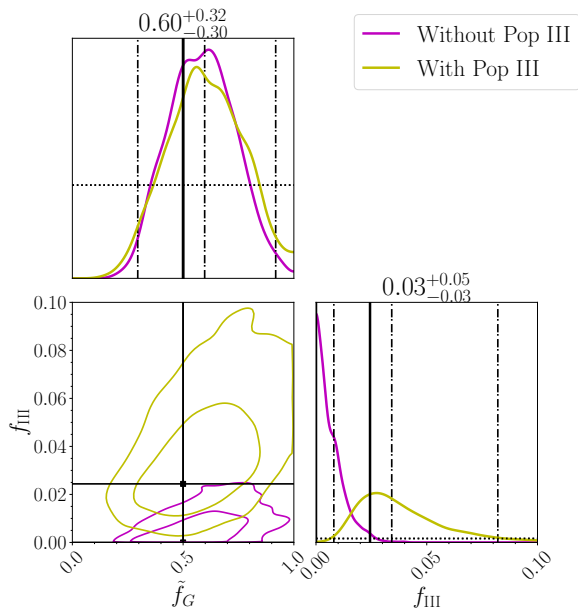


FIG. 9. Hyper-posterior of the population fractions, $(\tilde{f}_G, f_{\text{III}})$, for the universe $(\tilde{f}_G, f_{\text{III}}) = (0.5, 0.024)$. The plot setting is the same as in Figs. 7 and 8.

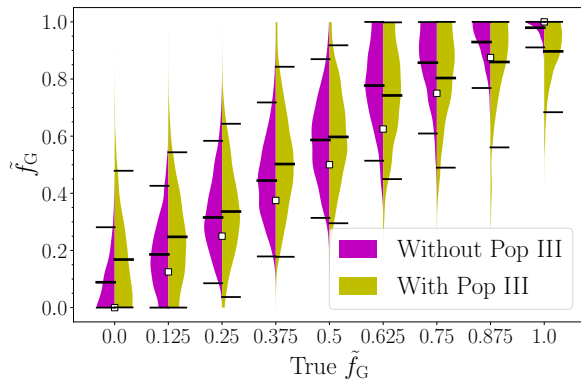


FIG. 10. Marginalized hyper-posteriors of \tilde{f}_G for all 18 universes, split into two categories: without (purple) and with (yellow) Pop III binaries. The plot setting is the same as in Fig. 4.

properties of different BBH populations using redshift-only information. The larger horizon of a 3G detector network allows accessing thousands of BBHs per month up to $z \sim 15$, which is necessary to resolve the excess of high-redshift ($z \gtrsim 8$) BBHs originated from Pop III stars. We consider ~ 16000 binaries, roughly corresponding to two months of data, and multiple values of the branching ratio between binary formation in galactic fields and globular clusters. For every value of this branching ratio, we analyzed both a case where a few hundred Pop III BBHs are present, and one where they don't exist.

First, we consider a hierarchical inference approach based on a nonparametric reconstruction of the total volumetric merger rate density \dot{n} . We look for local peaks in

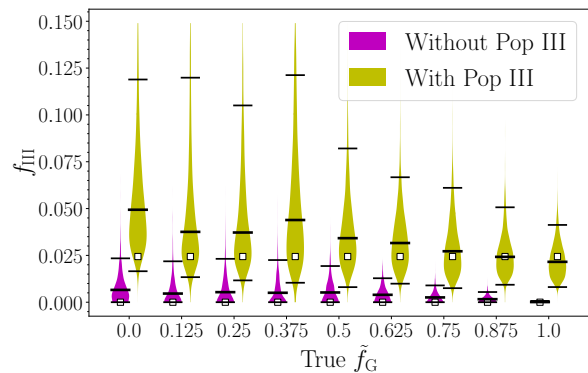


FIG. 11. Marginalized hyper-posteriors of f_{III} for all 18 universes. The plot setting is the same as in Fig. 4.

the reconstructed total merger rate, and extract limited but useful information about the high-redshift population. By requiring that a possible high-redshift peak has an amplitude of at least 1/10 of the low-redshift peak, we find evidence for the presence of an high-redshift peak when Pop III binaries are added, and constrain its position to be in the range $7 \leq z_h \leq 15$ for various mixing fractions between field and cluster binaries. Using the same approach, we rule out the existence of secondary-peak structure if there were no Pop III binaries. This minimally modeled measurement of the position of an high-redshift peak (or lack thereof) in the total binary merger rate might, with some model, be translated into an measurement or an upper limit on the abundance of Pop III stars. With a similar approach, we are able to measure the position of a low-redshift peak, which might be used to investigate typical time delays between start formation and mergers.

Then, we considered a modeled analysis where a phenomenological model exist for each of the three subpopulations, which are characterized by a set of unknown hyper-parameters, measured from the data together with the (unknown) branching ratios. Among the most remarkable results, we found that irrespective of the true value of the relative abundances of field and cluster binaries, the Pop III fraction can be constrained to be $f_{\text{III}} \gtrsim 0.01$ ($f_{\text{III}} \lesssim 0.02$) at 95% credibility for the universes that have (do not have) Pop III binaries. In both cases, the branching ratio between field and cluster binaries can be measured with better than $\sim 50\%$ uncertainty (95% credible interval). The precision on the measurement of the Pop III population mainly depends on the morphology of the merger rate densities of the dominating channels in the high-redshift region. If the dominating channels predict a shallower declining slope at high redshift, an eventual contribution to the high-redshift merger rate from the Pop III population is less distinctive, introducing correlations with the dominating channels.

We emphasize that our analysis is only assuming two months worth of data. A back-of-the-envelope calculation assuming that the statistical uncertainty shrinks like

$1/\sqrt{N}$ would imply a factor of ~ 5 improvement over the results we present here, after 5 years of data. In that scenario, the phenomenological approach could identify a fraction of Pop III mergers as small as $f_{\text{III}} \sim 0.5\%$. However, as stressed multiple times in this work, the phenomenological inference requires reliable models for the merger rate of the various formation channels, and will yield results which are as good as the models. On the other hand, the model independent approach, though intrinsically less precise, has the attractive feature of not requiring any specific modeling of the underlying subpopulation.

In this work, we have only considered three subpopulations: the galactic field and cluster binaries, as well as high-redshift Pop III binaries. As mentioned above, many other channels have been proposed and can plausibly contribute a sizeable fraction of the total rate. Our analysis can be trivially extended to include these and other subpopulations, at the price of increasing computational cost, correlations, and potentially degrading the measurement of some of the parameters. On the other hand, most of these different channels predict distinctive features in the BBHs they produce, beside their redshift distribution, for example masses, spins and eccentricity [13, 60, 81–98, 100–105]. Including these features can enhance the precision of multi-population inference, help fighting correlations, and improve the understanding of each formation channel. We leave this extension of multi-dimensional BBH parameters in the 3G era as a future work.

ACKNOWLEDGMENTS

The authors would like to thank Emanuele Berti, Hsin-Yu Chen, Carl Haster, and the LVK’s rate and population working group for fruitful discussions and comments. K.N. and S.V. acknowledge support of the National Science Foundation through the NSF award PHY-1836814. K.N. and S.V. are members of the LIGO Laboratory. W.M.F. is funded by the Center for Computational Astrophysics at the Flatiron Institute, which is supported by the Simons Foundation. LIGO was constructed by the California Institute of Technology and Massachusetts Institute of Technology with funding from the National Science Foundation and operates under cooperative agreement PHY-1764464. This paper carries LIGO document number LIGO-P2000540.

Appendix A: Gaussian process regression

This section provides details on the implementation of the GRP that we use to infer \dot{n} without assuming any specific functional form. We only require that $d\dot{N}/dz$ is sufficiently smooth such that $d\dot{N}/dz$ can be described by a piecewise-constant function over $W = 30$ redshift bins, which are uniformly distributed in linear space in the range $0 \leq z \leq 15$. The merger rate $d\dot{N}/dz$ is thus written

as

$$\frac{d\dot{N}}{dz} = \begin{cases} \frac{\Delta\dot{N}_1}{\Delta z_1} & 0 \leq z < z_1 \\ \dots & \\ \frac{\Delta\dot{N}_i}{\Delta z_i} & z_{i-1} \leq z < z_i \\ \dots & \\ \frac{\Delta\dot{N}_W}{\Delta z_W} & z_{W-1} \leq z < z_W \end{cases}, \quad (\text{A1})$$

where $\Delta\dot{N}_i$ is the merger rate in i -th redshift bin $\Delta z_i \equiv z_i - z_{i-1} = 0.5$ so that $\sum_{i=1}^W (\Delta\dot{N}_i) \equiv \dot{N}$. To make the GPR more efficient, we infer $d\dot{N}/dz$ in natural-log space. Then, we apply a squared-exponential Gaussian process prior on $X_i \equiv \ln(\Delta\dot{N}_i)$, with a covariance kernel

$$K_{ij} \equiv \text{Cov}(X_i, X_j) = \sigma_X^2 \exp \left[-\frac{1}{2} \left(\frac{z_{i-1/2} - z_{j-1/2}}{l} \right)^2 \right], \quad (\text{A2})$$

where $z_{i-1/2} = \frac{1}{2}(z_i - z_{i-1})$ is the midpoint of the i -th redshift bin, σ_X^2 is the variance of $\{X_i\}$, and l is the correlation length in redshift space. The multivariate Gaussian process prior on the random variable vector $\mathbf{X} \equiv \{\ln(\Delta\dot{N}_i)\}$ with a mean vector $\boldsymbol{\mu}_X$ and a covariance matrix $\mathbf{K} \equiv \{K_{ij}\}$ is then,

$$\mathcal{G}(\mathbf{X} | \boldsymbol{\mu}_X, \sigma_X, l) \equiv \mathcal{N}[\mathbf{X} | \boldsymbol{\mu}_X, \mathbf{K}(\sigma_X, l)]. \quad (\text{A3})$$

The kernel \mathbf{K} enforces the smoothness of $d\dot{N}/dz$ on scales that are comparable to or larger than l , which may be much larger than the bin spacing if the data support it, and prevents from over-fitting when W is large [123]. To further enhance the sampling efficiency, we utilize the Cholesky factorization to decompose \mathbf{K} into a lower-triangular matrix \mathbf{L} such that

$$\mathbf{X} \equiv \boldsymbol{\mu}_X + \mathbf{L}(\sigma_X, l)\boldsymbol{\eta} \quad (\text{A4})$$

follows the same Gaussian process prior \mathcal{G} by drawing $\boldsymbol{\eta}$ from a multivariate standard normal distribution. A common choice of $\boldsymbol{\mu}_X$ is a constant mean vector $\mu_X \mathbf{1}$. Since we know that $d\dot{N}/dz$ has a strong dependence of the redshifted differential comoving volume $dV_c/dz/(1+z)$, we further impose the mean of the Gaussian process prior to be the natural log of $dV_c/dz/(1+z)$ (normalized to N_{obs} within the comoving volume V_c and the observation time T) with a common shift $\Delta\mu_X$, i.e.

$$\{\mu_{X,i}\} = \left\{ \ln \left(\frac{N_{\text{obs}}}{V_c T} \int_{z_{i-1}}^{z_i} \frac{dV_c}{dz} dz \right) + \Delta\mu_X \right\}, \quad (\text{A5})$$

and we treat $\Delta\mu_X$, which is a single variable, as an additional parameter to include any possible fluctuation in the normalization \dot{N} . We then obtain \dot{n} from $d\dot{N}/dz$ divided by the differential volume in each bin. Altogether, the $W + 3 = 33$ hyper-parameters in the Gaussian process regression are thus

$$\boldsymbol{\Lambda}_{\text{GPR}} = (\{\eta_i\}_{i=1}^W, \Delta\mu_X, \sigma_X, l). \quad (\text{A6})$$

Appendix B: Phenomenological model

Directly modeling the volumetric merger rate \dot{n} of a sub-population as a function of astrophysical quantities, such as various distributions of initial stellar mass, mass/radius of star clusters, BH natal kicks, or stellar metallicity, requires detailed stellar evolution or N-body simulations which are computationally expensive. To facilitate our analysis, we model the three formation channels phenomenologically. For field, we follow the Madau-Dickinson functional form ³:

$$\dot{n}_F(z | \alpha_F, \beta_F, C_F) \propto \frac{(1+z)^{\alpha_F}}{1 + \left(\frac{1+z}{C_F}\right)^{\beta_F}}, \quad (\text{B1})$$

where α_F , β_F and C_F are unknown parameters that characterize the upward slope at $z \lesssim C_F - 1$, the downward slope at $z \gtrsim C_F - 1$, and the peak location of the volumetric merger rate density, respectively.

For cluster binaries, we describe the volumetric merger rate as a log-normal distribution in cosmic time, which we treat as a function of redshift:

$$\dot{n}_G(z | \mu_G, \sigma_G, t_G) \propto \text{LogNorm}(t(z) - t_G | \mu_G, \sigma_G), \quad (\text{B2})$$

where $t(z)$ is the cosmic time as a function of redshift, and LogNorm is the standard lognormal distribution of the argument $t - t_G$ parameterized by μ_G and σ_G . The additional parameter, t_G , is a reference time that mark the birth of the first cluster binaries.

For Pop III, we use the following functional form:

$$\dot{n}_{\text{III}}(z | a_{\text{III}}, b_{\text{III}}, z_{\text{III}}) \propto \frac{e^{a_{\text{III}}(z-z_{\text{III}})}}{a_{\text{III}} + b_{\text{III}}e^{(a_{\text{III}}+b_{\text{III}})(z-z_{\text{III}})}}, \quad (\text{B3})$$

where a_{III} , b_{III} and z_{III} characterize the upward slope at $z < z_{\text{III}}$, the downward slope at $z > z_{\text{III}}$, and the peak location of the volumetric merger rate density, respectively.

We have verified that these three phenomenological models can fit well the data from population synthesis analysis [58, 95, 103] for values of their arguments given in Eqs. (B1), (B2) and (B3).

We define the branching ratio between field and cluster binaries, f_G implicitly through the equations:

$$f_G \equiv \tilde{f}_G (1 - f_{\text{III}}), \quad (\text{B4})$$

$$f_F \equiv \left(1 - \tilde{f}_G\right) (1 - f_{\text{III}}), \quad (\text{B5})$$

where $\{f_k\}$ are the original fractions of Eq. (4).

Therefore, there are a total of 12 hyper-parameters in the phenomenological model:

$$\Lambda_{\text{PM}} = \left(\alpha_F, \beta_F, C_F, \mu_G, \sigma_G, t_G, a_{\text{III}}, b_{\text{III}}, z_{\text{III}}, \tilde{f}_G, f_{\text{III}}, \dot{N} \right). \quad (\text{B6})$$

Appendix C: Hyper-priors

The priors of all of the Λ_{GPR} hyper-parameters are tabulated in Table. I.

TABLE I. Hyper-priors for the GPR model.

$\Lambda_{\text{GPR},i}$	Prior function	Prior parameters	Domain
η_i	Normal	$(\mu_N, \sigma_N) = (0, 1)$	$(-\infty, +\infty)$
$\Delta\mu_X$	Normal	$(\mu_N, \sigma_N) = (0, 10)$	$(-\infty, +\infty)$
σ_X	Lognormal	$(\mu_{\text{LN}}, \sigma_{\text{LN}}) = (0, 4)$	$(0, +\infty)$
l	Lognormal	$(\mu_{\text{LN}}, \sigma_{\text{LN}}) = (0, \frac{1}{2} \ln(10))$	$(0, +\infty)$

The priors of all the Λ_{PM} hyper-parameters are tabulated in Table. II. The choice of lognormal priors is made

TABLE II. Hyper-priors for the phenomenological models.

$\Lambda_{\text{PM},i}$	Prior function	Prior parameters	Domain
α_F	Lognormal	$(\mu_{\text{LN}}, \sigma_{\text{LN}}) = (\hat{\alpha}_F, 0.25)$ ^a	$(0, 10]$
β_F	Lognormal	$(\mu_{\text{LN}}, \sigma_{\text{LN}}) = (\hat{\beta}_F, 0.25)$	$(0, 20]$
C_F	Lognormal	$(\mu_{\text{LN}}, \sigma_{\text{LN}}) = (\hat{C}_F, 0.25)$	$(0, 6]$
μ_G	Lognormal	$(\mu_{\text{LN}}, \sigma_{\text{LN}}) = (\hat{\mu}_G, 0.25)$	$(0, 5]$
σ_G	Lognormal	$(\mu_{\text{LN}}, \sigma_{\text{LN}}) = (\hat{\sigma}_G, 0.25)$	$(0, 5]$
t_G	Lognormal	$(\mu_{\text{LN}}, \sigma_{\text{LN}}) = (\hat{t}_G, 0.25)$	$(0, 2.0]$
a_{III}	Lognormal	$(\mu_{\text{LN}}, \sigma_{\text{LN}}) = (\hat{a}_{\text{III}}, 0.5)$	$(0, 2]$
b_{III}	Lognormal	$(\mu_{\text{LN}}, \sigma_{\text{LN}}) = (\hat{b}_{\text{III}}, 1)$	$(0, 2]$
z_{III}	Normal	$(\mu_N, \sigma_N) = (\hat{z}_{\text{III}}, 2)$ ^b	$[8, 20]$
f_{III}	Uniform	—	$[0, 0.5]$
\tilde{f}_G	Uniform	—	$[0, 1.0]$
\dot{N}	Half Cauchy	$\gamma_C = N_{\text{obs}}$ ^c	$[0, +\infty]$

^a μ_{LN} and σ_{LN} are the mean and standard deviation of the lognormal distribution, respectively.

^b μ_N and σ_N are the mean and standard deviation of the normal distribution, respectively.

^c γ_C is the scale parameter of the Cauchy distribution.

to restrict each model always carrying a characteristic peak within the redshift range, rather than increasing or decreasing monotonically. The gaussian prior and the domain of z_{III} ensure that the peak of \dot{n}_{III} lies at high redshift $z \geq 8$ and prevents \dot{n}_{III} from mimicking the two dominating channels which have peaks at low redshift $z \lesssim 3$.

- [1] J. Aasi *et al.* (LIGO Scientific), Advanced LIGO, *Class. Quant. Grav.* **32**, 074001 (2015), [arXiv:1411.4547 \[gr-qc\]](#).
- [2] F. Acernese *et al.* (VIRGO), Advanced Virgo: a second-generation interferometric gravitational wave detector, *Class. Quant. Grav.* **32**, 024001 (2015), [arXiv:1408.3978 \[gr-qc\]](#).
- [3] Y. Aso, Y. Michimura, K. Somiya, M. Ando, O. Miyakawa, T. Sekiguchi, D. Tatsumi, and H. Yamamoto (KAGRA), Interferometer design of the KAGRA gravitational wave detector, *Phys. Rev. D* **88**, 043007 (2013), [arXiv:1306.6747 \[gr-qc\]](#).
- [4] B. Abbott *et al.* (LIGO Scientific, Virgo), GWTC-1: A Gravitational-Wave Transient Catalog of Compact Binary Mergers Observed by LIGO and Virgo during the First and Second Observing Runs, *Phys. Rev. X* **9**, 031040 (2019), [arXiv:1811.12907 \[astro-ph.HE\]](#).
- [5] R. Abbott *et al.* (LIGO Scientific, Virgo), GWTC-2: Compact Binary Coalescences Observed by LIGO and Virgo During the First Half of the Third Observing Run, *arXiv e-print* (2020), [arXiv:2010.14527 \[gr-qc\]](#).
- [6] B. Abbott *et al.* (LIGO Scientific, Virgo), Binary Black Hole Population Properties Inferred from the First and Second Observing Runs of Advanced LIGO and Advanced Virgo, *Astrophys. J. Lett.* **882**, L24 (2019), [arXiv:1811.12940 \[astro-ph.HE\]](#).
- [7] R. Abbott *et al.* (LIGO Scientific, Virgo), Population Properties of Compact Objects from the Second LIGO-Virgo Gravitational-Wave Transient Catalog, *arXiv e-print* (2020), [arXiv:2010.14533 \[astro-ph.HE\]](#).
- [8] W. M. Farr, S. Stevenson, M. Coleman Miller, I. Mandel, B. Farr, and A. Vecchio, Distinguishing Spin-Aligned and Isotropic Black Hole Populations With Gravitational Waves, *Nature* **548**, 426 (2017), [arXiv:1706.01385 \[astro-ph.HE\]](#).
- [9] M. Zevin, C. Pankow, C. L. Rodriguez, L. Sampson, E. Chase, V. Kalogera, and F. A. Rasio, Constraining Formation Models of Binary Black Holes with Gravitational-Wave Observations, *Astrophys. J.* **846**, 82 (2017), [arXiv:1704.07379 \[astro-ph.HE\]](#).
- [10] K. W. Wong, K. Breivik, K. Kremer, and T. Callister, Joint constraints on the field-cluster mixing fraction, common envelope efficiency, and globular cluster radii from a population of binary hole mergers via deep learning, *arXiv e-print* (2020), [arXiv:2011.03564 \[astro-ph.HE\]](#).
- [11] M. Zevin, S. S. Bavera, C. P. Berry, V. Kalogera, T. Fragos, P. Marchant, C. L. Rodriguez, F. Antonini, D. E. Holz, and C. Pankow, One Channel to Rule Them All? Constraining the Origins of Binary Black Holes using Multiple Formation Pathways, *arXiv e-print* (2020), [arXiv:2011.10057 \[astro-ph.HE\]](#).
- [12] T. Callister, W. Farr, and M. Renzo, State of the field: Binary black hole spins, natal kicks, and prospects for isolated field formation after GWTC-2, *arXiv e-print* (2020), [arXiv:2011.09570 \[astro-ph.HE\]](#).
- [13] F. Antonini and M. Gieles, Merger rate of black hole binaries from globular clusters: theoretical error bars and comparison to gravitational wave data, *arXiv e-print* (2020), [arXiv:2009.01861 \[astro-ph.HE\]](#).
- [14] K. Belczynski *et al.*, Evolutionary roads leading to low effective spins, high black hole masses, and O1/O2 rates for LIGO/Virgo binary black holes, *Astron. Astrophys.* **636**, A104 (2020), [arXiv:1706.07053 \[astro-ph.HE\]](#).
- [15] M. Fishbach, D. E. Holz, and B. Farr, Are LIGO's Black Holes Made From Smaller Black Holes?, *Astrophys. J. Lett.* **840**, L24 (2017), [arXiv:1703.06869 \[astro-ph.HE\]](#).
- [16] D. Gerosa and E. Berti, Are merging black holes born from stellar collapse or previous mergers?, *Phys. Rev. D* **95**, 124046 (2017), [arXiv:1703.06223 \[gr-qc\]](#).
- [17] Z. Doctor, D. Wysocki, R. O'Shaughnessy, D. E. Holz, and B. Farr, Black Hole Coagulation: Modeling Hierarchical Mergers in Black Hole Populations, *ArXiv e-print* 10.3847/1538-4357/ab7fac (2019), [arXiv:1911.04424 \[astro-ph.HE\]](#).
- [18] C. Kimball, C. P. Berry, and V. Kalogera, What GW170729's exceptional mass and spin tells us about its family tree, *ArXiv e-print* 10.3847/2515-5172/ab66be (2019), [arXiv:1903.07813 \[astro-ph.HE\]](#).
- [19] C. Kimball *et al.*, Evidence for hierarchical black hole mergers in the second LIGO-Virgo gravitational-wave catalog, *arXiv e-print* (2020), [arXiv:2011.05332 \[astro-ph.HE\]](#).
- [20] D. Gerosa, S. Vitale, and E. Berti, Astrophysical implications of GW190412 as a remnant of a previous black-hole merger, *Phys. Rev. Lett.* **125**, 101103 (2020), [arXiv:2005.04243 \[astro-ph.HE\]](#).
- [21] V. Tiwari and S. Fairhurst, The Emergence of Structure in the Binary Black Hole Mass Distribution, *ArXiv e-print* (2020), [arXiv:2011.04502 \[astro-ph.HE\]](#).
- [22] R. Farmer, M. Renzo, S. de Mink, M. Fishbach, and S. Justham, Constraints on gravitational wave detections of binary black hole mergers on the $^{12}\text{C}(\alpha, \gamma)^{16}\text{O}$ rate, *Astrophys. J. Lett.* **902**, L36 (2020), [arXiv:2006.06678 \[astro-ph.HE\]](#).
- [23] G. Fragione and A. Loeb, Implications of recoil kicks for black hole mergers from LIGO/Virgo catalogs, *ArXiv e-print* (2020), [arXiv:2011.08935 \[astro-ph.HE\]](#).
- [24] S. S. Bavera *et al.*, The impact of mass-transfer physics on the observable properties of field binary black hole populations, *ArXiv e-print* (2020), [arXiv:2010.16333 \[astro-ph.HE\]](#).
- [25] Y. Ali-Haïmoud, E. D. Kovetz, and M. Kamionkowski, Merger rate of primordial black-hole binaries, *Phys. Rev. D* **96**, 123523 (2017), [arXiv:1709.06576 \[astro-ph.CO\]](#).
- [26] S. Bird, I. Cholis, J. B. Muñoz, Y. Ali-Haïmoud, M. Kamionkowski, E. D. Kovetz, A. Raccanelli, and A. G. Riess, Did LIGO detect dark matter?, *Phys. Rev. Lett.* **116**, 201301 (2016), [arXiv:1603.00464 \[astro-ph.CO\]](#).
- [27] M. Sasaki, T. Suyama, T. Tanaka, and S. Yokoyama, Primordial Black Hole Scenario for the Gravitational-Wave Event GW150914, *Phys. Rev. Lett.* **117**, 061101 (2016), [Erratum: *Phys.Rev.Lett.* 121, 059901 (2018)], [arXiv:1603.08338 \[astro-ph.CO\]](#).
- [28] K. Wong, G. Franciolini, V. De Luca, V. Baibhav, E. Berti, P. Pani, and A. Riotto, Constraining the primordial black hole scenario with Bayesian inference and

³ Note that while we use the same *form* for the equation, we do *not* assume that the numerical coefficients are the same of the standard Madau-Dickinson SFR

- machine learning: the GWTC-2 gravitational wave catalog, ArXiv e-print (2020), [arXiv:2011.01865 \[gr-qc\]](#).
- [29] A. Hall, A. D. Gow, and C. T. Byrnes, Bayesian analysis of LIGO-Virgo mergers: Primordial vs. astrophysical black hole populations, ArXiv e-print (2020), [arXiv:2008.13704 \[astro-ph.CO\]](#).
- [30] C. Boehm, A. Kobakhidze, C. A. O’Hare, Z. S. Picker, and M. Sakellariadou, Eliminating the LIGO bounds on primordial black hole dark matter, ArXiv e-print (2020), [arXiv:2008.10743 \[astro-ph.CO\]](#).
- [31] A. Arvanitaki, M. Baryakhtar, S. Dimopoulos, S. Dubovsky, and R. Lasenby, Black Hole Mergers and the QCD Axion at Advanced LIGO, *Phys. Rev. D* **95**, 043001 (2017), [arXiv:1604.03958 \[hep-ph\]](#).
- [32] R. Brito, S. Ghosh, E. Barausse, E. Berti, V. Cardoso, I. Dvorkin, A. Klein, and P. Pani, Gravitational wave searches for ultralight bosons with LIGO and LISA, *Phys. Rev. D* **96**, 064050 (2017), [arXiv:1706.06311 \[gr-qc\]](#).
- [33] K. K. Ng, O. A. Hannuksela, S. Vitale, and T. G. Li, Searching for ultralight bosons within spin measurements of a population of binary black hole mergers, arXiv e-print (2019), [arXiv:1908.02312 \[gr-qc\]](#).
- [34] K. K. Ng, S. Vitale, O. A. Hannuksela, and T. G. Li, Constraints on ultralight scalar bosons within black hole spin measurements from LIGO-Virgo’s GWTC-2, arXiv e-print (2020), [arXiv:2011.06010 \[gr-qc\]](#).
- [35] S. Vitale, R. Lynch, R. Sturani, and P. Graff, Use of gravitational waves to probe the formation channels of compact binaries, *Class. Quant. Grav.* **34**, 03LT01 (2017), [arXiv:1503.04307 \[gr-qc\]](#).
- [36] S. Stevenson, F. Ohme, and S. Fairhurst, Distinguishing compact binary population synthesis models using gravitational-wave observations of coalescing binary black holes, *Astrophys. J.* **810**, 58 (2015), [arXiv:1504.07802 \[astro-ph.HE\]](#).
- [37] B. Farr, D. E. Holz, and W. M. Farr, Using Spin to Understand the Formation of LIGO and Virgo’s Black Holes, *Astrophys. J. Lett.* **854**, L9 (2018), [arXiv:1709.07896 \[astro-ph.HE\]](#).
- [38] M. Fishbach and D. E. Holz, Where Are LIGO’s Big Black Holes?, *Astrophys. J. Lett.* **851**, L25 (2017), [arXiv:1709.08584 \[astro-ph.HE\]](#).
- [39] M. Fishbach, W. M. Farr, and D. E. Holz, The Most Massive Binary Black Hole Detections and the Identification of Population Outliers, *Astrophys. J. Lett.* **891**, L31 (2020), [arXiv:1911.05882 \[astro-ph.HE\]](#).
- [40] C. Kimball, C. Talbot, C. P. L. Berry, M. Carney, M. Zevin, E. Thrane, and V. Kalogera, Black Hole Genealogy: Identifying Hierarchical Mergers with Gravitational Waves, *Astrophys. J.* **900**, 177 (2020), [arXiv:2005.00023 \[astro-ph.HE\]](#).
- [41] C. Talbot and E. Thrane, Determining the population properties of spinning black holes, *Phys. Rev. D* **96**, 023012 (2017), [arXiv:1704.08370 \[astro-ph.HE\]](#).
- [42] C. Talbot and E. Thrane, Measuring the binary black hole mass spectrum with an astrophysically motivated parameterization, *Astrophys. J.* **856**, 173 (2018), [arXiv:1801.02699 \[astro-ph.HE\]](#).
- [43] Y. Bouffanais, M. Mapelli, D. Gerosa, U. N. Di Carlo, N. Giacobbo, E. Berti, and V. Baibhav, Constraining the fraction of binary black holes formed in isolation and young star clusters with gravitational-wave data, *Astrophys. J.* **886**, 10.3847/1538-4357/ab4a79 (2019), [arXiv:1905.11054 \[astro-ph.HE\]](#).
- [44] S. Miller, T. A. Callister, and W. Farr, The Low Effective Spin of Binary Black Holes and Implications for Individual Gravitational-Wave Events, *Astrophys. J.* **895**, 128 (2020), [arXiv:2001.06051 \[astro-ph.HE\]](#).
- [45] M. Safarzadeh, W. M. Farr, and E. Ramirez-Ruiz, A trend in the effective spin distribution of LIGO binary black holes with mass, *Astrophys. J.* **894**, 129 (2020), [arXiv:2001.06490 \[gr-qc\]](#).
- [46] M. Fishbach and D. E. Holz, Minding the gap: GW190521 as a straddling binary, ArXiv e-print 10.3847/2041-8213/abc827 (2020), [arXiv:2009.05472 \[astro-ph.HE\]](#).
- [47] M. E. Lower, E. Thrane, P. D. Lasky, and R. Smith, Measuring eccentricity in binary black hole inspirals with gravitational waves, *Phys. Rev. D* **98**, 083028 (2018), [arXiv:1806.05350 \[astro-ph.HE\]](#).
- [48] M. Fishbach, D. E. Holz, and W. M. Farr, Does the Black Hole Merger Rate Evolve with Redshift?, *Astrophys. J. Lett.* **863**, L41 (2018), [arXiv:1805.10270 \[astro-ph.HE\]](#).
- [49] T. Callister, M. Fishbach, D. Holz, and W. Farr, Shouts and Murmurs: Combining Individual Gravitational-Wave Sources with the Stochastic Background to Measure the History of Binary Black Hole Mergers, *Astrophys. J. Lett.* **896**, L32 (2020), [arXiv:2003.12152 \[astro-ph.HE\]](#).
- [50] J. Roulet, T. Venumadhav, B. Zackay, L. Dai, and M. Zaldarriaga, Binary Black Hole Mergers from LIGO/Virgo O1 and O2: Population Inference Combining Confident and Marginal Events, arXiv e-print (2020), [arXiv:2008.07014 \[astro-ph.HE\]](#).
- [51] T. Venumadhav, B. Zackay, J. Roulet, L. Dai, and M. Zaldarriaga, New binary black hole mergers in the second observing run of Advanced LIGO and Advanced Virgo, *Phys. Rev. D* **101**, 083030 (2020), [arXiv:1904.07214 \[astro-ph.HE\]](#).
- [52] L. McCuller *et al.*, Frequency-Dependent Squeezing for Advanced LIGO, *Phys. Rev. Lett.* **124**, 171102 (2020), [arXiv:2003.13443 \[astro-ph.IM\]](#).
- [53] H. Yu *et al.*, Prospects for detecting gravitational waves at 5 Hz with ground-based detectors, *Phys. Rev. Lett.* **120**, 141102 (2018), [arXiv:1712.05417 \[astro-ph.IM\]](#).
- [54] B. P. Abbott *et al.*, Sensitivity of the Advanced LIGO detectors at the beginning of gravitational wave astronomy, *Phys. Rev. D* **93**, 112004 (2016), [Addendum: *Phys. Rev. D* **97**, 059901 (2018)], [arXiv:1604.00439 \[astro-ph.IM\]](#).
- [55] E. D. Hall and M. Evans, Metrics for next-generation gravitational-wave detectors, *Class. Quant. Grav.* **36**, 225002 (2019), [arXiv:1902.09485 \[astro-ph.IM\]](#).
- [56] T. Kinugawa, K. Inayoshi, K. Hotokezaka, D. Nakauchi, and T. Nakamura, Possible Indirect Confirmation of the Existence of Pop III Massive Stars by Gravitational Wave, *Mon. Not. Roy. Astron. Soc.* **442**, 2963 (2014), [arXiv:1402.6672 \[astro-ph.HE\]](#).
- [57] T. Kinugawa, A. Miyamoto, N. Kanda, and T. Nakamura, The detection rate of inspiral and quasi-normal modes of Population III binary black holes which can confirm or refute the general relativity in the strong gravity region, *Mon. Not. Roy. Astron. Soc.* **456**, 1093 (2016), [arXiv:1505.06962 \[astro-ph.SR\]](#).
- [58] K. Belczynski, T. Ryu, R. Perna, E. Berti, T. Tanaka, and T. Bulik, On the likelihood of detecting gravitational waves from Population III compact object binaries, *Mon. Not. Roy. Astron. Soc.* **471**, 4702 (2017),

- arXiv:1612.01524 [astro-ph.HE].
- [59] T. Hartwig, M. Volonteri, V. Bromm, R. S. Klessen, E. Barausse, M. Magg, and A. Stacy, Gravitational Waves from the Remnants of the First Stars, *Mon. Not. Roy. Astron. Soc.* **460**, L74 (2016), arXiv:1603.05655 [astro-ph.GA].
- [60] M. Raidal, C. Spethmann, V. Vaskonen, and H. Veermäe, Formation and Evolution of Primordial Black Hole Binaries in the Early Universe, *JCAP* **02**, 018, arXiv:1812.01930 [astro-ph.CO].
- [61] R. Abbott *et al.* (LIGO Scientific, Virgo), GW190521: A Binary Black Hole Merger with a Total Mass of $150M_{\odot}$, *Phys. Rev. Lett.* **125**, 101102 (2020), arXiv:2009.01075 [gr-qc].
- [62] R. Abbott *et al.* (LIGO Scientific, Virgo), Properties and Astrophysical Implications of the $150M_{\odot}$ Binary Black Hole Merger GW190521, *Astrophys. J. Lett.* **900**, L13 (2020), arXiv:2009.01190 [astro-ph.HE].
- [63] T. Kinugawa, T. Nakamura, and H. Nakano, Formation of Binary Black Holes Similar to GW190521 with a Total Mass of $\sim 150M_{\odot}$ from Population III Binary Star Evolution, arXiv e-print (2020), arXiv:2009.06922 [astro-ph.HE].
- [64] A. Tanikawa, T. Kinugawa, T. Yoshida, K. Hijikawa, and H. Umeda, Population III Binary Black Holes: Effects of Convective Overshooting on Formation of GW190521, arXiv e-print (2020), arXiv:2010.07616 [astro-ph.HE].
- [65] B. P. Abbott *et al.* (LIGO Scientific), Exploring the Sensitivity of Next Generation Gravitational Wave Detectors, *Class. Quant. Grav.* **34**, 044001 (2017), arXiv:1607.08697 [astro-ph.IM].
- [66] D. Reitze *et al.*, Cosmic Explorer: The U.S. Contribution to Gravitational-Wave Astronomy beyond LIGO, *Bull. Am. Astron. Soc.* **51**, 035 (2019), arXiv:1907.04833 [astro-ph.IM].
- [67] C. Van Den Broeck, Compact binary coalescence and the science case for Einstein Telescope, in *On recent developments in theoretical and experimental general relativity, astrophysics and relativistic field theories. Proceedings, 12th Marcel Grossmann Meeting on General Relativity, Paris, France, July 12-18, 2009. Vol. 1-3* (2010) pp. 1682-1685, arXiv:1003.1386 [gr-qc].
- [68] M. Punturo *et al.*, The Einstein Telescope: A third-generation gravitational wave observatory, *Class. Quant. Grav.* **27**, 194002 (2010).
- [69] M. Maggiore *et al.*, Science Case for the Einstein Telescope, *JCAP* **03**, 050, arXiv:1912.02622 [astro-ph.CO].
- [70] J. E. Greene, J. Strader, and L. C. Ho, Intermediate-Mass Black Holes, *Annual Reviews of Astronomy & Astrophysics* **58**, 257 (2020), arXiv:1911.09678 [astro-ph.GA].
- [71] P. Amaro-Seoane *et al.* (LISA), Laser Interferometer Space Antenna, ArXiv e-print (2017), arXiv:1702.00786 [astro-ph.IM].
- [72] J. A. Gaskin *et al.*, Lynx X-Ray Observatory: an overview, *Journal of Astronomical Telescopes, Instruments, and Systems* **5**, 1 (2019).
- [73] T. Regimbau, M. Evans, N. Christensen, E. Katsavounidis, B. Sathyaprakash, and S. Vitale, Digging deeper: Observing primordial gravitational waves below the binary black hole produced stochastic background, *Phys. Rev. Lett.* **118**, 151105 (2017), arXiv:1611.08943 [astro-ph.CO].
- [74] S. Vitale, Three observational differences for binary black holes detections with second and third generation gravitational-wave detectors, *Phys. Rev. D* **94**, 121501 (2016), arXiv:1610.06914 [gr-qc].
- [75] S. Vitale and M. Evans, Parameter estimation for binary black holes with networks of third generation gravitational-wave detectors, *Phys. Rev. D* **95**, 064052 (2017), arXiv:1610.06917 [gr-qc].
- [76] S. Vitale and C. Whittle, Characterization of binary black holes by heterogeneous gravitational-wave networks, *Phys. Rev. D* **98**, 024029 (2018), arXiv:1804.07866 [gr-qc].
- [77] C. Van Den Broeck, Astrophysics, cosmology, and fundamental physics with compact binary coalescence and the Einstein Telescope, *J. Phys. Conf. Ser.* **484**, 012008 (2014), arXiv:1303.7393 [gr-qc].
- [78] S. Vitale, W. M. Farr, K. Ng, and C. L. Rodriguez, Measuring the star formation rate with gravitational waves from binary black holes, *Astrophys. J. Lett.* **886**, L1 (2019), arXiv:1808.00901 [astro-ph.HE].
- [79] M. Safarzadeh, E. Berger, K. K.-Y. Ng, H.-Y. Chen, S. Vitale, C. Whittle, and E. Scannapieco, Measuring the delay time distribution of binary neutron stars. II. Using the redshift distribution from third-generation gravitational wave detectors network, *Astrophys. J. Lett.* **878**, L13 (2019), arXiv:1904.10976 [astro-ph.HE].
- [80] I. M. Romero-Shaw, K. Kremer, P. D. Lasky, E. Thrane, and J. Samsing, Gravitational Waves as a Probe of Globular Cluster Formation and Evolution, arXiv e-print (2020), arXiv:2011.14541 [astro-ph.HE].
- [81] I. Bartos, B. Kocsis, Z. Haiman, and S. Márka, Rapid and Bright Stellar-mass Binary Black Hole Mergers in Active Galactic Nuclei, *Astrophys. J.* **835**, 165 (2017), arXiv:1602.03831 [astro-ph.HE].
- [82] S.-X. Yi and K. Cheng, Where Are the Electromagnetic-wave Counterparts of Stellar-mass Binary Black Hole Mergers?, *Astrophys. J. Lett.* **884**, L12 (2019), arXiv:1909.08384 [astro-ph.HE].
- [83] Y. Yang *et al.*, Hierarchical Black Hole Mergers in Active Galactic Nuclei, *Phys. Rev. Lett.* **123**, 181101 (2019), arXiv:1906.09281 [astro-ph.HE].
- [84] Y. Yang, I. Bartos, Z. Haiman, B. Kocsis, S. Márka, and H. Tagawa, Cosmic Evolution of Stellar-mass Black Hole Merger Rate in Active Galactic Nuclei, *Astrophys. J.* **896**, 138 (2020), arXiv:2003.08564 [astro-ph.HE].
- [85] M. Gröbner, W. Ishibashi, S. Tiwari, M. Haney, and P. Jetzer, Binary black hole mergers in AGN accretion discs: gravitational wave rate density estimates, *Astron. Astrophys.* **638**, A119 (2020), arXiv:2005.03571 [astro-ph.GA].
- [86] H. Tagawa, Z. Haiman, and B. Kocsis, Formation and Evolution of Compact Object Binaries in AGN Disks, *Astrophys. J.* **898**, 25 (2020), arXiv:1912.08218 [astro-ph.GA].
- [87] H. Tagawa, B. Kocsis, Z. Haiman, I. Bartos, K. Omukai, and J. Samsing, Mass-gap Mergers in Active Galactic Nuclei, arXiv e-print (2020), arXiv:2012.00011 [astro-ph.HE].
- [88] H. Tagawa, Z. Haiman, I. Bartos, and B. Kocsis, Spin Evolution of Stellar-mass Black Hole Binaries in Active Galactic Nuclei, *Astrophys. J.* **899**, 26 (2020), arXiv:2004.11914 [astro-ph.HE].
- [89] J. Samsing, I. Bartos, D. D’Orazio, Z. Haiman, B. Kocsis, N. Leigh, B. Liu, M. Pessah, and H. Tagawa, Active Galactic Nuclei as Factories for Eccentric Black Hole

- Mergers, Arxiv e-print (2020), [arXiv:2010.09765](https://arxiv.org/abs/2010.09765) [astro-ph.HE].
- [90] R. O’Shaughnessy, J. Bellovary, A. Brooks, S. Shen, F. Governato, and C. Christensen, The effects of host galaxy properties on merging compact binaries detectable by LIGO, *Mon. Not. Roy. Astron. Soc.* **464**, 2831 (2017), [arXiv:1609.06715](https://arxiv.org/abs/1609.06715) [astro-ph.GA].
- [91] M. Dominik, K. Belczynski, C. Fryer, D. Holz, E. Berti, T. Bulik, I. Mandel, and R. O’Shaughnessy, Double Compact Objects I: The Significance of the Common Envelope on Merger Rates, *Astrophys. J.* **759**, 52 (2012), [arXiv:1202.4901](https://arxiv.org/abs/1202.4901) [astro-ph.HE].
- [92] M. Dominik, K. Belczynski, C. Fryer, D. E. Holz, E. Berti, T. Bulik, I. Mandel, and R. O’Shaughnessy, Double Compact Objects II: Cosmological Merger Rates, *Astrophys. J.* **779**, 72 (2013), [arXiv:1308.1546](https://arxiv.org/abs/1308.1546) [astro-ph.HE].
- [93] M. Dominik, E. Berti, R. O’Shaughnessy, I. Mandel, K. Belczynski, C. Fryer, D. E. Holz, T. Bulik, and F. Pannarale, Double Compact Objects III: Gravitational Wave Detection Rates, *Astrophys. J.* **806**, 263 (2015), [arXiv:1405.7016](https://arxiv.org/abs/1405.7016) [astro-ph.HE].
- [94] S. de Mink and K. Belczynski, Merger rates of double neutron stars and stellar origin black holes: The Impact of Initial Conditions on Binary Evolution Predictions, *Astrophys. J.* **814**, 58 (2015), [arXiv:1506.03573](https://arxiv.org/abs/1506.03573) [astro-ph.HE].
- [95] K. Belczynski, D. E. Holz, T. Bulik, and R. O’Shaughnessy, The first gravitational-wave source from the isolated evolution of two 40-100 Msun stars, *Nature* **534**, 512 (2016), [arXiv:1602.04531](https://arxiv.org/abs/1602.04531) [astro-ph.HE].
- [96] M. Mapelli, N. Giacobbo, F. Santoliquido, and M. C. Artale, The properties of merging black holes and neutron stars across cosmic time, *Mon. Not. Roy. Astron. Soc.* **487**, 2 (2019), [arXiv:1902.01419](https://arxiv.org/abs/1902.01419) [astro-ph.HE].
- [97] K. Breivik *et al.*, COSMIC Variance in Binary Population Synthesis, *Astrophys. J.* **898**, 71 (2020), [arXiv:1911.00903](https://arxiv.org/abs/1911.00903) [astro-ph.HE].
- [98] S. Stevenson, A. Vigna-Gómez, I. Mandel, J. W. Barrett, C. J. Neijssel, D. Perkins, and S. E. de Mink, Formation of the first three gravitational-wave observations through isolated binary evolution, *Nature Commun.* **8**, 14906 (2017), [arXiv:1704.01352](https://arxiv.org/abs/1704.01352) [astro-ph.HE].
- [99] S. F. Portegies Zwart and S. L. W. McMillan, Black Hole Mergers in the Universe, *ApJ* **528**, L17 (2000), [arXiv:astro-ph/9910061](https://arxiv.org/abs/astro-ph/9910061) [astro-ph].
- [100] F. Santoliquido, M. Mapelli, N. Giacobbo, Y. Bouffanais, and M. C. Artale, The cosmic merger rate density of compact objects: impact of star formation, metallicity, initial mass function and binary evolution, arXiv e-print (2020), [arXiv:2009.03911](https://arxiv.org/abs/2009.03911) [astro-ph.HE].
- [101] C. L. Rodriguez, M. Morscher, B. Pattabiraman, S. Chatterjee, C.-J. Haster, and F. A. Rasio, Binary Black Hole Mergers from Globular Clusters: Implications for Advanced LIGO, *Phys. Rev. Lett.* **115**, 051101 (2015), [Erratum: *Phys.Rev.Lett.* 116, 029901 (2016)], [arXiv:1505.00792](https://arxiv.org/abs/1505.00792) [astro-ph.HE].
- [102] C. L. Rodriguez, S. Chatterjee, and F. A. Rasio, Binary Black Hole Mergers from Globular Clusters: Masses, Merger Rates, and the Impact of Stellar Evolution, *Phys. Rev. D* **93**, 084029 (2016), [arXiv:1602.02444](https://arxiv.org/abs/1602.02444) [astro-ph.HE].
- [103] C. L. Rodriguez and A. Loeb, Redshift Evolution of the Black Hole Merger Rate from Globular Clusters, *Astrophys. J. Lett.* **866**, L5 (2018), [arXiv:1809.01152](https://arxiv.org/abs/1809.01152) [astro-ph.HE].
- [104] U. N. Di Carlo, N. Giacobbo, M. Mapelli, M. Pasquato, M. Spera, L. Wang, and F. Haardt, Merging black holes in young star clusters, *Mon. Not. Roy. Astron. Soc.* **487**, 2947 (2019), [arXiv:1901.00863](https://arxiv.org/abs/1901.00863) [astro-ph.HE].
- [105] K. Kremer, M. Spera, D. Becker, S. Chatterjee, U. N. Di Carlo, G. Fragione, C. L. Rodriguez, C. S. Ye, and F. A. Rasio, Populating the upper black hole mass gap through stellar collisions in young star clusters, *Astrophys. J.* **903**, 45 (2020), [arXiv:2006.10771](https://arxiv.org/abs/2006.10771) [astro-ph.HE].
- [106] B. J. Carr and S. Hawking, Black holes in the early Universe, *Mon. Not. Roy. Astron. Soc.* **168**, 399 (1974).
- [107] S. Clesse and J. García-Bellido, The clustering of massive Primordial Black Holes as Dark Matter: measuring their mass distribution with Advanced LIGO, *Phys. Dark Univ.* **15**, 142 (2017), [arXiv:1603.05234](https://arxiv.org/abs/1603.05234) [astro-ph.CO].
- [108] E. Vangioni, K. Olive, T. Prestegard, J. Silk, P. Petitjean, and V. Mandic, The Impact of Star Formation and Gamma-Ray Burst Rates at High Redshift on Cosmic Chemical Evolution and Reionization, *Mon. Not. Roy. Astron. Soc.* **447**, 2575 (2015), [arXiv:1409.2462](https://arxiv.org/abs/1409.2462) [astro-ph.GA].
- [109] P. Madau and M. Dickinson, Cosmic Star Formation History, *Ann. Rev. Astron. Astrophys.* **52**, 415 (2014), [arXiv:1403.0007](https://arxiv.org/abs/1403.0007) [astro-ph.CO].
- [110] R. S. de Souza, N. Yoshida, and K. Ioka, Population III.1 and III.2 Gamma-Ray Bursts: Constraints on the Event Rate for Future Radio and X-ray Surveys, *Astron. Astrophys.* **533**, A32 (2011), [arXiv:1105.2395](https://arxiv.org/abs/1105.2395) [astro-ph.CO].
- [111] I. Baraffe, A. Heger, and S. Woosley, On the stability of very massive primordial stars, *Astrophys. J.* **550**, 890 (2001), [arXiv:astro-ph/0009410](https://arxiv.org/abs/astro-ph/0009410).
- [112] R. X. Adhikari *et al.*, Astrophysical science metrics for next-generation gravitational-wave detectors, *Class. Quant. Grav.* **36**, 245010 (2019), [arXiv:1905.02842](https://arxiv.org/abs/1905.02842) [astro-ph.HE].
- [113] K. El-Badry, E. Quataert, D. R. Weisz, N. Choksi, and M. Boylan-Kolchin, The formation and hierarchical assembly of globular cluster populations, *MNRAS* **482**, 4528 (2019), [arXiv:1805.03652](https://arxiv.org/abs/1805.03652) [astro-ph.GA].
- [114] M. Morscher, B. Pattabiraman, C. Rodriguez, F. A. Rasio, and S. Umbreit, The Dynamical Evolution of Stellar Black Holes in Globular Clusters, *ApJ* **800**, 9 (2015), [arXiv:1409.0866](https://arxiv.org/abs/1409.0866) [astro-ph.GA].
- [115] W. M. Farr, J. R. Gair, I. Mandel, and C. Cutler, Counting And Confusion: Bayesian Rate Estimation With Multiple Populations, *Phys. Rev. D* **91**, 023005 (2015), [arXiv:1302.5341](https://arxiv.org/abs/1302.5341) [astro-ph.IM].
- [116] I. Mandel, W. M. Farr, and J. R. Gair, Extracting distribution parameters from multiple uncertain observations with selection biases, *Mon. Not. Roy. Astron. Soc.* **486**, 1086 (2019), [arXiv:1809.02063](https://arxiv.org/abs/1809.02063) [physics.data-an].
- [117] E. Thrane and C. Talbot, An introduction to Bayesian inference in gravitational-wave astronomy: parameter estimation, model selection, and hierarchical models, *Publ. Astron. Soc. Austral.* **36**, e010 (2019), [Erratum: *Publ.Astron.Soc.Austral.* 37, e036 (2020)], [arXiv:1809.02293](https://arxiv.org/abs/1809.02293) [astro-ph.IM].
- [118] D. Wysocki, J. Lange, and R. O’Shaughnessy, Reconstructing phenomenological distributions of compact binaries via gravitational wave observations, *Phys. Rev. D* **100**, 043012 (2019), [arXiv:1805.06442](https://arxiv.org/abs/1805.06442) [gr-qc].

- [119] S. Vitale, One, No One, and One Hundred Thousand – Inferring the properties of a population in presence of selection effects, arXiv e-print (2020), [arXiv:2007.05579 \[astro-ph.IM\]](#).
- [120] I. Mandel, W. M. Farr, A. Colonna, S. Stevenson, P. Tiño, and J. Veitch, Model-independent inference on compact-binary observations, *Mon. Not. Roy. Astron. Soc.* **465**, 3254 (2017), [arXiv:1608.08223 \[astro-ph.HE\]](#).
- [121] P. Ade *et al.* (Planck), Planck 2015 results. XIII. Cosmological parameters, *Astron. Astrophys.* **594**, A13 (2016), [arXiv:1502.01589 \[astro-ph.CO\]](#).
- [122] M. Chruslinska, G. Nelemans, and K. Belczynski, The influence of the distribution of cosmic star formation at different metallicities on the properties of merging double compact objects, *Mon. Not. Roy. Astron. Soc.* **482**, 5012 (2019), [arXiv:1811.03565 \[astro-ph.HE\]](#).
- [123] D. Foreman-Mackey, D. W. Hogg, and T. D. Morton, Exoplanet Population Inference and the Abundance of Earth Analogs from Noisy, Incomplete Catalogs, *ApJ* **795**, 64 (2014), [arXiv:1406.3020 \[astro-ph.EP\]](#).